






Approaching the activity limit of CoSe_2 for oxygen evolution via Fe doping and Co vacancy

Yuhai Dou ¹, Chun-Ting He², Lei Zhang¹, Huajie Yin ¹, Mohammad Al-Mamun ¹, Jianmin Ma³ & Huijun Zhao ^{1,4} 

Electronic structure engineering lies at the heart of efficient catalyst design. Most previous studies, however, utilize only one technique to modulate the electronic structure, and therefore optimal electronic states are hard to be achieved. In this work, we incorporate both Fe dopants and Co vacancies into atomically thin CoSe_2 nanobelts for /coxygen evolution catalysis, and the resulted $\text{CoSe}_2\text{-D}_{\text{Fe}}\text{-V}_{\text{Co}}$ exhibits much higher catalytic activity than other defect-activated CoSe_2 and previously reported FeCo compounds. Deep characterizations and theoretical calculations identify the most active center of Co_2 site that is adjacent to the V_{Co} -nearest surface Fe site. Fe doping and Co vacancy synergistically tune the electronic states of Co_2 to a near-optimal value, resulting in greatly decreased binding energy of OH^* (ΔE_{OH^*}) without changing ΔE_{O} , and consequently lowering the catalytic overpotential. The proper combination of multiple defect structures is promising to unlock the catalytic power of different catalysts for various electrochemical reactions.

¹Centre for Clean Environment and Energy, Gold Coast Campus, Griffith University, Gold Coast QLD 4222, Australia. ²Key Laboratory of Functional Small Organic Molecule, Ministry of Education, College of Chemistry and Chemical Engineering, Jiangxi Normal University, Nanchang, Jiangxi 330022, China. ³School of Physics and Electronics, Hunan University, Changsha, Hunan 410082, China. ⁴Centre for Environmental and Energy Nanomaterials, CAS Centre for Excellence in Nanoscience, Institute of Solid State Physics, Chinese Academy of Sciences, Hefei, Anhui 230031, China. ✉email: h.zhao@griffith.edu.au

Design of highly efficient water splitting electrocatalysts for clean hydrogen production is essential for the sustainable development of modern society^{1,2}. Electronic structure engineering via incorporating dopants, vacancies, strains, heterostructures, etc. lies at the heart of efficient catalyst design, as it effectively tunes the binding energies of reaction intermediates^{3,4}. Most previous studies, however, utilize only one technique to manipulate the electronic structure, and thus the catalytic performance is barely satisfactory^{5,6}. For instance, CoSe₂ has moderate catalytic activity toward oxygen evolution reaction (OER), and the doping of Fe has been demonstrated to be an effective approach to improving the performance^{7,8}. However, whether the activity could be further enhanced in a synergetic manner by incorporating other defects, such as anion and cation vacancies, has not been reported. We believe that the proper combination of two or more defect structures is essential to achieve near optimal electronic states and ideal intermediate binding energies, which holds the key for the construction of highly efficient water splitting electrocatalysts.

In this work, we seek to fully excavate the catalytic potential of atomically thin CoSe₂ nanobelts for OER by incorporating Fe dopants and Co/Se vacancies. Through both experiments and theoretical calculations, we find that the best catalyst is CoSe₂-D_{Fe}-V_{Co} and the most active center is the Co₂ site adjacent to the V_{Co}-nearest surface Fe site. Fe doping and Co vacancy work synergistically to optimize the electronic states of Co₂, and therefore the binding energy of OH* is dramatically decreased and high catalytic activity is achieved. By contrast, Se-derived O vacancy has an obvious impact on the binding energy of O* at Co₂ site, which results in relatively high overpotential and low catalytic activity.

Results

Synthesis and structural characterization. Figure 1a shows the synthetic strategies of different electrocatalysts. Firstly, CoSe₂ nuclei were assembled with diethylenetriamine (DETA) under hydrothermal reaction, leading to the formation of CoSe₂/DETA

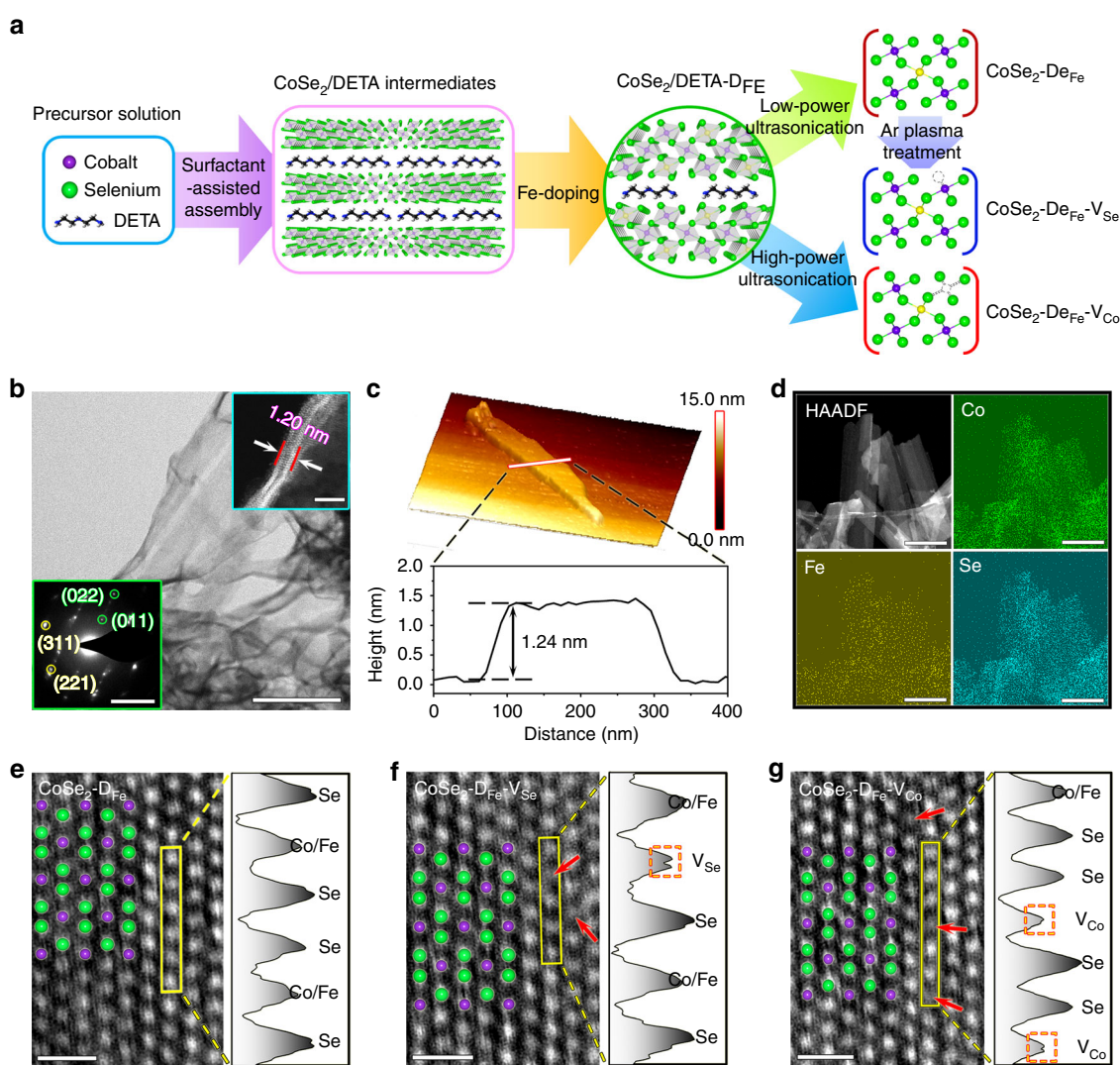


Fig. 1 Synthesis and structural characterization of CoSe₂-D_{Fe}, CoSe₂-D_{Fe}-V_{Se}, and CoSe₂-D_{Fe}-V_{Co}. **a** Schematic illustration of the synthetic methods for different catalysts. **b** Scanning transmission electron microscopy (STEM) image of CoSe₂-D_{Fe}-V_{Co} nanobelts with selected area electron diffraction pattern (left inset) indicating the mixed cubic and orthorhombic phases and cross-sectional view (right inset) showing the atomic thickness. Scale bar, 200 nm, 5 1/nm (left inset) and 2 nm (right inset). **c** Atomic force microscopy image of CoSe₂-D_{Fe}-V_{Co} and height profile along the white line in the image. **d** Elemental maps of Co, Fe, and Se in CoSe₂-D_{Fe}-V_{Co}. Scale bar, 300 nm. **e–g** High-resolution high-angle annular dark-field STEM (HAADF-STEM) images of different catalysts and the intensity profiles along the selected rectangular regions suggest the missed surface Se and Co atoms in CoSe₂-D_{Fe}-V_{Se} and CoSe₂-D_{Fe}-V_{Co}, respectively. Scale bar, 0.5 nm.

lamellar intermediates⁹. Fe ions were then incorporated into CoSe₂/DETA via a wet-impregnation method involving chemical adsorption and cation exchange¹⁰. After that, atomically thin CoSe₂-D_{Fe} nanobelts were obtained by liquid-phase exfoliation using low-power ultrasonication. Se vacancies were created on the surface of exfoliated CoSe₂-D_{Fe} nanobelts through Ar plasma treatment¹¹, and Co vacancies were extracted by DETA molecules during the exfoliation of CoSe₂/DETA under high ultrasonic power¹². Figure 1b shows the scanning transmission electron microscopy (STEM) image of the CoSe₂-D_{Fe}-V_{Co} nanobelts. The selected area electron diffraction (SAED) pattern (left inset) reveals the coexistence of cubic (yellow) and orthorhombic (green) phases of CoSe₂ matrix, which is also identified by the X-ray diffraction (XRD) patterns (Supplementary Fig. 1)¹³. The cross-sectional view of the nanobelts (right inset) suggests an atomic thickness of ~1.20 nm, which is further confirmed by the atomic force microscopy analysis (Fig. 1c). Energy dispersive X-ray spectroscopy (EDS) mapping shows that Co, Se, and Fe dopants are homogeneous distributed throughout the nanobelts (Fig. 1d). The doping ratio of Fe to total cation content is about 18.3% according to the inductively coupled plasma atomic emission spectroscopy (ICP-AES) results (Supplementary Table 1). A certain amount of O was also detected by EDS analysis (Supplementary Fig. 2), attributing to the deviation of Se/Co ratio from the stoichiometry of CoSe₂ that results from the low solubility of Na₂SeO₃ in H₂O-DETA mixed solvent^{13,14}. The presence of oxides was also evidenced by Raman spectroscopy (Supplementary Fig. 3), where the peak at 164 cm⁻¹ corresponds to the stretching mode of Se-Se in CoSe₂¹², and the peaks at 190, 515, 612, 472, and 676 cm⁻¹ are assigned to the F_{2g}(1), F_{2g}(2), F_{2g}(3), E_g, and A_{1g} modes of CoO_x, respectively¹⁵. The created Se and Co vacancies are readily visible via high-angle annular dark-field STEM (HAADF-STEM) imaging (Fig. 1e-g). In addition, the intensity profiles along the selected rectangular regions also suggest the missed surface Se and Co atoms in CoSe₂-D_{Fe}-V_{Se} and CoSe₂-D_{Fe}-V_{Co}, respectively.

OER catalytic activity evaluation. To understand how Fe dopants and Co/Se vacancies affect the OER catalytic performance, the prepared catalysts were subjected to systematic electrochemical evaluation via the rotating disk electrode (RDE) method in purified 1 M NaOH (Fig. 2). Cyclic voltammetry (CV) was first conducted to activate the electrodes (Supplementary Fig. 4), and large current densities were recorded during the first few cycles, indicating the instability of CoSe₂ in alkaline solution at anodic potentials¹⁴. EDS analysis shows that Se signal can hardly be detected after CV test, and SAED pattern indicates the formation of CoOOH phase, which serves as the real host under OER conditions (Supplementary Fig. 5). The thickness of the nanobelts increases from 1.24 to 1.35 nm after CV activation (Supplementary Fig. 6), which is resulted from the significantly increased surface roughness due to CV-induced structural reconstruction.

The catalytic activities were then assessed by linear sweep voltammetry (LSV, Fig. 2a). The polarization curves were corrected with 95% iR-compensation and then normalized by the electrochemical double-layer capacitance. As shown in Fig. 2b, c, to reach a current density (*j*) of 2.5 A F⁻¹, the required overpotentials (η) for CoSe₂, CoSe₂-D_{Fe}, CoSe₂-D_{Fe}-V_{Se}, and CoSe₂-D_{Fe}-V_{Co} are 385.7, 300.4, 307.3, and 294.2 mV, respectively, and at $\eta = 350$ mV, the recorded *j* are 0.92, 8.73, 7.06, and 12.95 A F⁻¹, respectively. Therefore, Fe doping, in accordance with previous reports, enhances the OER catalytic performance of CoSe₂, and further incorporation of Se and Co vacancies leads to slightly decreased and dramatically increased catalytic activity,

respectively. It is important to note that the current density achieved by CoSe₂-D_{Fe}-V_{Co} at $\eta = 350$ mV is 30.2% higher than the sum of the current densities of CoSe₂-D_{Fe} and CoSe₂-V_{Co} (Supplementary Fig. 7), indicating a synergistic effect between Fe dopants and Co vacancies. This synergistic effect was further confirmed by changing the sequence of Fe doping and Co vacancy. As shown in Supplementary Fig. 8, the CoSe₂-V_{Co}-D_{Fe} exhibits higher overpotential and lower current density than CoSe₂-D_{Fe}-V_{Co}, probably due to that the afterward doping fills the vacancy sites and weakens the role of Co vacancies¹⁶.

The high catalytic activity of CoSe₂-D_{Fe}-V_{Co} was further evidenced by analyzing the turnover frequency (TOF, assuming all cations to be catalytically active) and Tafel slope (derived from the polarization curve in low overpotential region). As shown in Fig. 2d, the apparent TOF of CoSe₂-D_{Fe}-V_{Co} at $\eta = 280$ mV reaches 0.045 s⁻¹, exceeding 0.003, 0.035, and 0.024 s⁻¹ for CoSe₂, CoSe₂-D_{Fe}, and CoSe₂-D_{Fe}-V_{Se}, respectively, indicative of the high intrinsic catalytic activity. In addition, CoSe₂-D_{Fe}-V_{Co} exhibits a small Tafel slope of 53.5 mV dec⁻¹, much lower than 72.6, 66.0, and 70.5 mV dec⁻¹ for CoSe₂, CoSe₂-D_{Fe} and CoSe₂-D_{Fe}-V_{Se}, respectively (Fig. 2e), suggesting the remarkably enhanced reaction kinetics⁶. The Nyquist plots at $\eta = 370$ mV display typical semicircles for different catalysts (Fig. 2f), corresponding to the charge transfer resistances (*R*_{ct}). Using a relevant equivalent circuit (inset), the fitted results indicate the smallest *R*_{ct} (4.2 Ω) of CoSe₂-D_{Fe}-V_{Co} compared with those of CoSe₂ (10.5 Ω), CoSe₂-D_{Fe} (5.3 Ω) and CoSe₂-D_{Fe}-V_{Se} (5.4 Ω), indicating the efficient electron transfer and the fast ion diffusion⁸. As a result, the incorporation of Fe dopants and Co vacancies creates highly active catalytic sites with excellent mass transport properties for OER catalysis.

It is also noteworthy that CoSe₂-D_{Fe}-V_{Co} outperforms commercial IrO₂ and RuO₂ electrodes (Supplementary Fig. 9), and previously reported CoSe₂ and FeCo compounds evaluated via the RDE method (Fig. 2g)¹⁷⁻²⁸. The outstanding performance is firstly attributable to the atomic thickness of the nanobelts, which provides abundant surface active sites for the catalytic reaction (Supplementary Fig. 10). In addition, the proper doping level of Fe optimizes the electrode composition and improves the catalytic performance (Supplementary Fig. 11). More importantly, Fe doping and Co vacancies work synergistically to create highly active centers and dramatically enhance the catalytic activity.

The catalytic stability was further assessed via chronoamperometry (CA) for 6 h and chronopotentiometry (CP) for 8 h. As shown in Fig. 2h, CA test shows that the current density increases with increasing overpotential. More specifically, CoSe₂-D_{Fe}-V_{Co} delivers average current densities of 30.5, 51.6, 76.3, 101.6 mA cm⁻² at $\eta = 370, 420, 470, 520$ mV, respectively, exceeding those of CoSe₂ (10.8, 26.9, 45.5, 66.3 mA cm⁻²), CoSe₂-D_{Fe} (24.6, 43.5, 64.5, 87.0 mA cm⁻²), and CoSe₂-D_{Fe}-V_{Se} (21.6, 39.8, 60.5, 80.5 mA cm⁻²). CP test at *j* = 10 mA cm⁻² shows that the overpotential of CoSe₂ suffers an obvious increase of 13.6 mV, while those of CoSe₂-D_{Fe}, CoSe₂-D_{Fe}-V_{Se}, and CoSe₂-D_{Fe}-V_{Co} see slight rises of 8.6, 7.0, and 3.7 mV, respectively, which should be attributed to the enhanced electrical conductivity caused by Fe doping²⁹. Generally, the trend in the activity of different catalysts does not change after long-term durability test.

Understanding defect structures before and after catalysis. Prior to the mechanism investigation, it is essential to study the stability of dopants and vacancies and probe the evolution of electronic structures during catalysis as they are directly relevant to the catalytic activity³⁰. X-ray photoelectron spectroscopy (XPS)

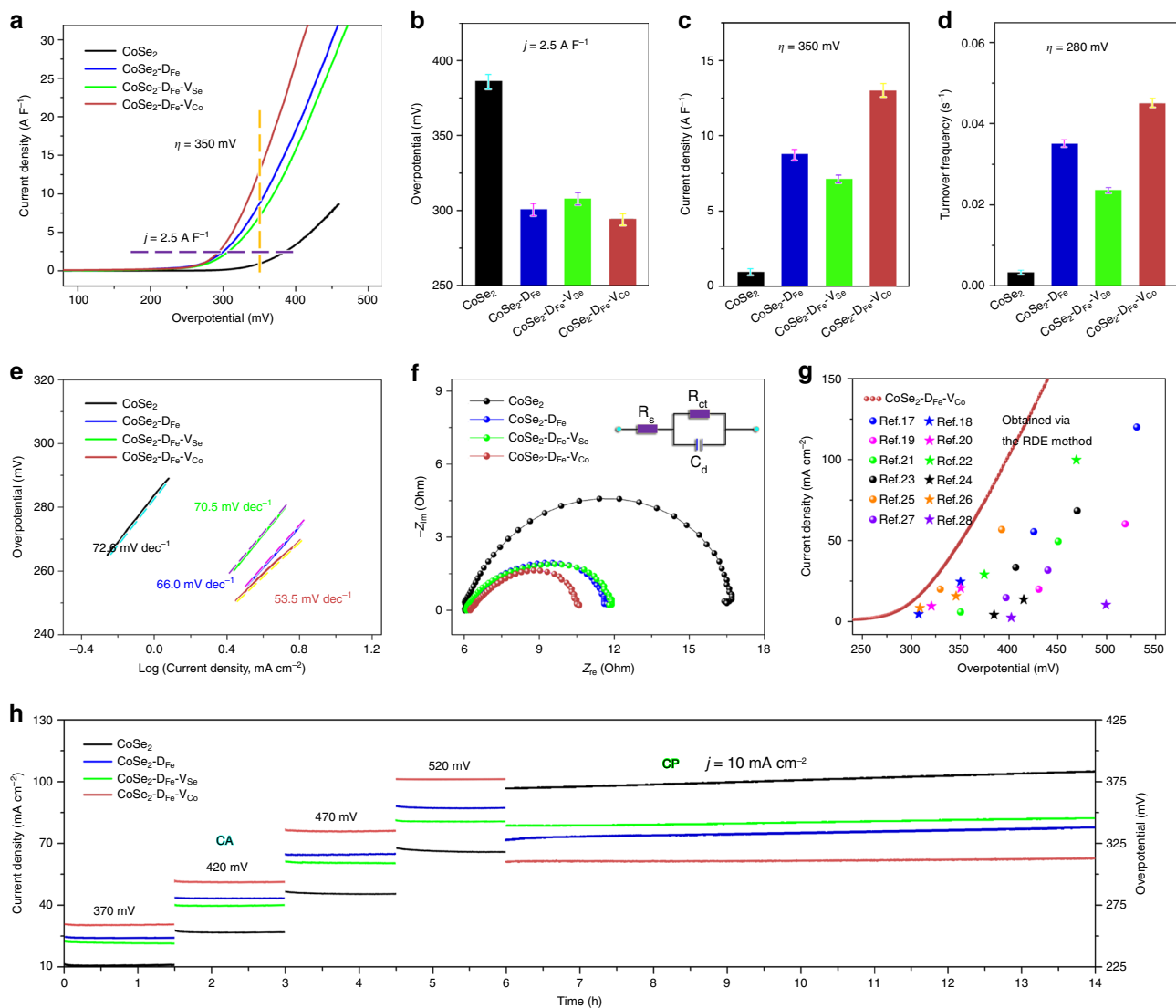


Fig. 2 Catalytic performance for the oxygen evolution reaction. **a** Linear sweep voltammograms normalized by electrochemical double-layer capacitance. **b** Overpotentials (η) required to reach a current density (j) of 2.5 A F^{-1} . **c** Current densities at $\eta = 350 \text{ mV}$. **d** Turnover frequencies calculated at $\eta = 280 \text{ mV}$. **e** Tafel plots derived from the polarization curves in low overpotential regions. **f** Nyquist plots at $\eta = 370 \text{ mV}$ with inset showing the equivalent circuit model. **g** Comparison of the catalytic performance between $\text{CoSe}_2\text{-D}_{\text{Fe}}\text{-V}_{\text{Co}}$ and previously reported CoSe_2 and FeCo compounds evaluated via the rotating disk electrode (RDE) method. **h** Durability evaluation via chronoamperometry test at stepwise η of 370, 420, 470, and 520 mV for 6 h, and chronopotentiometry test at $j = 10 \text{ mA cm}^{-2}$ for 8 h. The error bars in **b-d** denote standard deviation of five technical replicates.

was first performed to understand the primary defects before catalysis. As shown in Fig. 3a, b and Supplementary Fig. 12, Co, Fe, and Se signals are clearly detected, indicating the successful doping of Fe into CoSe_2 matrix, and the Co/Fe 2p spectra show the existence of Co/Fe–O bonds due to oxide impurities. The Co/Fe 2p_{3/2} peaks of Co/Fe–Se and Co/Fe–O in $\text{CoSe}_2\text{-D}_{\text{Fe}}\text{-V}_{\text{Se}}$ exhibit negative shifts to lower binding energies, and those in $\text{CoSe}_2\text{-D}_{\text{Fe}}\text{-V}_{\text{Co}}$ show positive shifts to higher binding energies, indicating the reduction and oxidation states of metal sites caused by Se/O and Co vacancies, respectively (Fig. 3c)³¹. The defect structures after CA test at $\eta = 370 \text{ mV}$ for 1.5 h were then investigated via electron energy loss spectroscopy (EELS). As shown in Fig. 3d, e, both Co and Fe signals can be detected after catalysis, and no significant changes in their atom ratios were found due to fully purified electrolyte (Supplementary Table 1). For better analysis, the L_{2,3}-edge spectra of Co and Fe were fitted by multiple Gaussian functions, which represent different oxidation states and coordination environments³². Compared with

$\text{CoSe}_2\text{-D}_{\text{Fe}}$, there are extra Gaussian peaks centered at 780.0 and 795.4 eV (cyan) in Co L_{2,3}-edge spectra, and 709.0 and 723.0 eV (purple) in Fe L_{2,3}-edge spectra of $\text{CoSe}_2\text{-D}_{\text{Fe}}\text{-V}_{\text{Se}}$, which most likely result from the Se-derived O vacancies. In comparison, extra peaks located at 783.0 and 797.9 eV (orange) in Co L_{2,3}-edge spectra, and 712.6 and 724.8 eV (magenta) in Fe L_{2,3}-edge spectra of $\text{CoSe}_2\text{-D}_{\text{Fe}}\text{-V}_{\text{Co}}$, which should be ascribed to the local chemical environment of Co vacancies. Therefore, the surface reconstruction induced by OER catalysis has little impact on the defect structures. To provide further evidence, X-ray absorption near-edge structure (XANES) spectra at the L-edges of Co and Fe before and after catalysis were conducted (Fig. 3f and Supplementary Fig. 13). Obviously, the L₃-edge centroids of Co before catalysis shift by 0.10 and 0.12 eV to lower and higher energy positions after the incorporation of Se/O and Co vacancies, respectively^{33,34}. After catalysis, slight broadenings of the white line peaks were observed due to OER-induced complex coordination environment³⁵. Despite the electronic-structure changes,

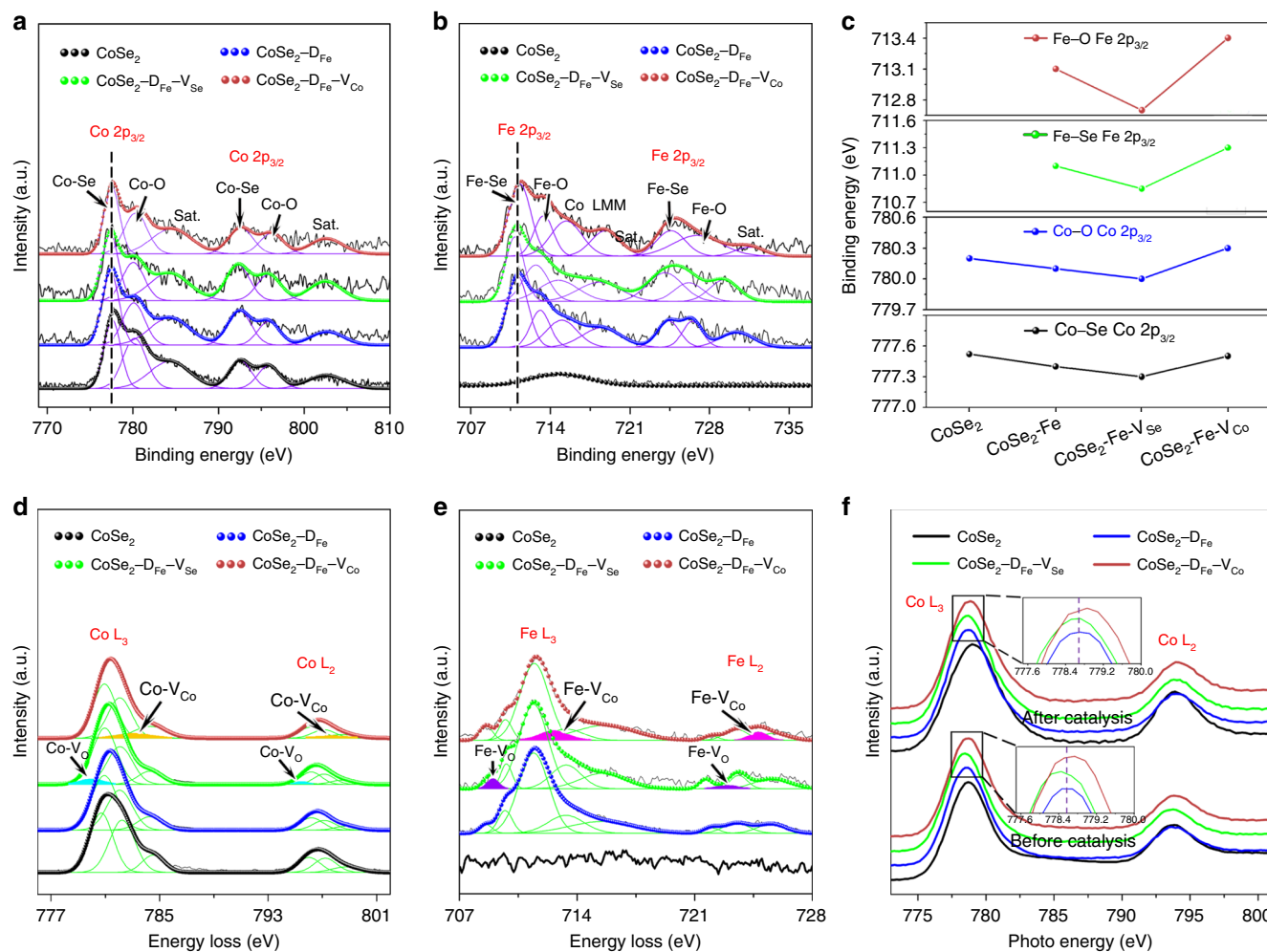


Fig. 3 Defect structure identification before and after catalysis. **a, b** Co 2p and Fe 2p X-ray photoelectron spectroscopy spectra of primary catalysts. **c** Binding energy shifts of Co–Se, Co–O, Fe–Se, and Fe–O peaks due to doping and vacancies. **d, e** Co and Fe L-edge electron energy loss spectra after chronoamperometry test at 370 mV for 1.5 h showing the existence of extra peaks in $\text{CoSe}_2\text{-D}_{\text{Fe}}\text{-V}_{\text{Se}}$ and $\text{CoSe}_2\text{-D}_{\text{Fe}}\text{-V}_{\text{Co}}$. **f** Co L-edge X-ray absorption near-edge structure spectra before and after catalysis showing the energy shifts caused by doping and vacancies.

the Co $L_{3\text{-edge}}$ centroids of $\text{CoSe}_2\text{-D}_{\text{Fe}}\text{-V}_{\text{Se}}$ and $\text{CoSe}_2\text{-D}_{\text{Fe}}\text{-V}_{\text{Co}}$ still exhibit 0.06 and 0.11 eV shifts to lower and higher energy positions, respectively. The same trends of energy shift could be obtained from the $L_{2,3\text{-edge}}$ XANES spectra of Fe (Supplementary Fig. 13). As a result, both dopants and vacancies are well preserved during OER catalysis, and they consequently determine the catalytic performance of different catalysts.

Discussion

To provide clear insight into the effects of dopants and vacancies on the catalytic activities, we performed Hubbard-corrected density functional theory (DFT + U) calculations. The crystal structure of CoOOH was utilized to build up the periodical surface models as it serves as the real host under OER conditions (Supplementary Figs. 4 and 5). The high-index (01-12) facet was selected as the surface termination due to the proved good coincidence between theoretical and experimental results³⁶, and all potential active sites on (01-12) facets of models with different atomistic arrangements of dopants and vacancies were considered to gain insight into the catalytic mechanism (Supplementary Fig. 14). Figure 4a shows the $\text{FeCoOOH-V}_{\text{Co}}$ structure and the OER pathway, which involves four proton coupled electron transfer steps and three intermediates of OH^* , O^* , and OOH^* ³⁷. The corresponding Gibbs free energies (ΔG_i , $i = \text{OH}^*$, O^* , and

OOH^*) were calculated and provided in Fig. 4b. As can be seen, the catalytic activities of Co sites are restricted by the transformation of OH^* to O^* , due to the relatively large difference between ΔG_{O^*} and ΔG_{OH^*} (namely ΔG_2). In comparison, the potential-limiting step of Fe sites is assigned to the transformation of O^* to OOH^* , owing to the relatively large difference between ΔG_{OOH^*} and ΔG_{O^*} (i.e., ΔG_3). Therefore, Co and Fe sites in CoOOH matrix exhibit different catalytic behaviors for OER. The ΔG_i of $\text{FeCoOOH-V}_{\text{O}}\text{-Co}_1$ and $\text{FeCoOOH-V}_{\text{Co}}\text{-Co}_1$ deviate from the general principle probably due to that they are adjacent to the vacancies and their electronic states are greatly altered.

Scaling relations exist between energetics of OH^* and OOH^* over the above considered metal sites^{36–38}, which are expressed as $\Delta G_{\text{OOH}^*} = \Delta G_{\text{OH}^*} + 2.90$ eV (Gibbs free energies, Fig. 4c), $\Delta E_{\text{OOH}^*} = \Delta E_{\text{OH}^*} + 2.87$ eV (adsorption energies, Supplementary Fig. 15a), and $\Delta E_{\text{OOH}} = \Delta E_{\text{OH}} + 1.03$ eV (binding energies, Supplementary Fig. 15b) (Supplementary Table 2). Based on the scaling relation, a universal volcano relationship can be constructed by plotting η^{OER} as a function of $\Delta G_{\text{O}^*} - \Delta G_{\text{OH}^*}$ ³⁸. As shown in Fig. 4d, Fe sites are distributed around the left leg of the volcano which is restricted by the transformation of O^* to OOH^* , and Co sites are located on the right leg that is determined by the transformation of OH^* to O^* . Both Fe and Co could serve as OER active centers by analyzing their η^{OER} , which

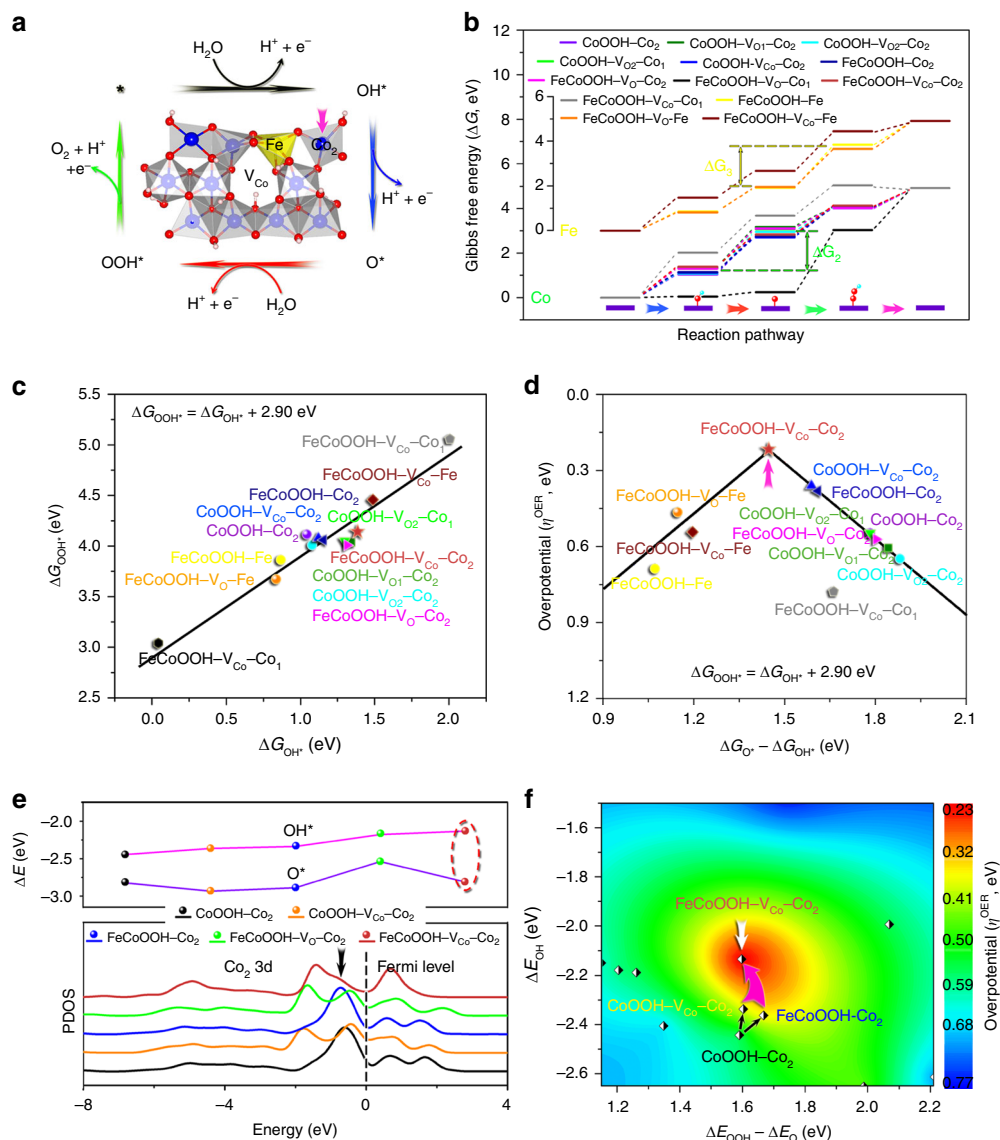


Fig. 4 Hubbard-corrected density functional theory calculations of catalytic activities of different surface metal sites. **a** Crystal structure of FeCoOOH-V_{Co} and oxygen evolution reaction reaction pathway on (01-12) facet. **b** Gibbs free energy profiles along the reaction pathway. **c** Scaling relation between ΔG_{OOH^+} and ΔG_{OH^+} . **d** Volcano plot of overpotential as a function of $\Delta G_{\text{O}^-} - \Delta G_{\text{OH}^+}$, based on the scaling relation. **e** Calculated partial density of states (PDOS) of Co₂ sites and binding energies of OH* and O*. **f** Contour plot of theoretical overpotential as a function of $\Delta E_{\text{OOH}} - \Delta E_{\text{O}}$ and ΔE_{OH} , indicating the near-optimal intermediate binding energies achieved by Fe doping and Co vacancy.

have been confirmed by previous studies^{26,39–41}. Among all considered metal sites in different models, however, the most active center is the Co₂ site that is adjacent to the vacancy-nearest surface Fe site in FeCoOOH-V_{Co}. By comparing the Co₂ of CoOOH, FeCoOOH, CoOOH-V_{Co} and FeCoOOH-V_{Co}, we can see that Fe doping and Co vacancy individually decrease the overpotential from 549 to 380 and 360 mV, respectively, while they jointly push Co₂ to the top of the volcano, leading to the lowest overpotential of 218 mV among all investigated metal sites. Therefore, the theoretical simulations successfully identify the most active catalytic sites and verify the synergistic effect between Fe dopants and Co vacancies.

To deeply understand how Fe doping and Co vacancy modulate the electronic states of Co₂ and consequently tune the intermediate binding energy, the partial density of states of Co₂ 3d in CoOOH, CoOOH-V_{Co}, FeCoOOH, FeCoOOH-V_{Co}, and FeCoOOH-V_{Co} were calculated. As shown in Fig. 4e, an intense negative peak near the Fermi level was observed in CoOOH. Fe

doping causes a small shift of the peak away from the Fermi level and Co vacancy induces the splitting of the peak, both of which lead to slightly decreased binding energy of OH*⁴². Remarkably, the combination of Fe doping and Co vacancy greatly decreases the peak intensity near the Fermi level, and therefore results in dramatically weakened binding with OH*. It is important to note that, the low overpotential is achieved due to that Fe doping and Co vacancy jointly have little impact on the binding energy of O* (dashed ellipse in Fig. 4e). In comparison, even though the combination of Fe doping and O vacancy decreases the binding energy of OH* as well, they have a more obvious influence on the binding energy of O*, which leads to increased overpotential and declined catalytic activity.

A contour plot of 3D overpotential surface as a function of $\Delta E_{\text{OOH}} - \Delta E_{\text{O}}$ and ΔE_{OH} can be constructed based on the calculated activities of different metal sites. As shown in Fig. 4f, the overpotential decreases along the direction: blue→cyan→green→yellow→red. CoOOH-Co₂ with a moderate overpotential locates

in the green region, and the incorporation of Fe doping and Co vacancy individually moves the point to the green–yellow boundary. FeCoOOH–V_{Co}–Co₂, sitting close to the center of the red region, possesses near-optimal intermediate binding energies, and near-minimum catalytic overpotential that different systems can research in this study. Therefore, Fe doping and Co vacancy work synergistically to approach the activity limit of Co-based catalysts. This contour map provides valuable guidance for the design of efficient OER catalysts via modulating the electronic structures and intermediate binding energies.

In conclusion, different defect structures were incorporated into atomically thin CoSe₂ nanobelts for OER catalysis. We found that the combination of Fe doping and Co vacancy synergistically optimize the electronic states and intermediate binding energies at Co₂ site, which is responsible for the dramatically enhanced catalytic activity. This electronic-structure modulation strategy with proper combination of two or more defect structures could efficiently unlock the catalytic power, showing great promise for the rational design of advanced catalysts for various electrochemical reactions.

Methods

Material synthesis. Atomically thin CoSe₂ nanobelts were synthesized via a lamellar intermediate-assisted exfoliation approach. In detail, 14.0 ml DETA was slowly poured into 7.0 ml H₂O under stirring as severe exothermic reaction occurs. Then, 0.125 g Co(Ac)₂·4H₂O and 0.130 g Na₂SeO₃ were added and stirred until completely dissolved. After that, hydrothermal reaction was performed at 160 °C for 10 h, and CoSe₂/DETA lamellar intermediates were finally obtained after reaction. Fe doping was performed by adding 1.0 ml of 0.025 mol L⁻¹ Fe(NO₃)₃·9H₂O aqueous solution into the CoSe₂/DETA intermediates solution, and atomically thin nanobelts were exfoliated from the intermediates in ethanol by using an ultrasonic homogenizer (on time: 2 s, off time: 1 s, output power: 12%, process time: 5 h). Se vacancies were created on the exfoliated Fe-doped CoSe₂ nanobelts via Ar plasma engraving with an irradiation time of 5 min, a power of 100 W, and a gas flow rate of 50 sccm. Co vacancies were incorporated during the exfoliation of Fe-doped CoSe₂/DETA intermediates under high-power ultrasonication (on time: 2 s, off time: 1 s, output power: 30%, process time: 2 h). The resulted dispersions were centrifuged at 1000 rmp for 10 min to remove the unexfoliated powders.

Characterizations. The morphology of nanobelts was observed via STEM (JEOL JEM-ARM200F), and the composition elements were identified by atomic-resolution elemental maps via EDS (Oxford XMax100TLE EDS spectrometer). The element contents before catalysis and after CA test at $\eta = 370$ mV for 1.5 h were determined by an Optima 2000 DV ICP-emission spectrometer. SAED, XRD (MMA, GBC Scientific Equipment LLC, Hampshire, IL, USA) and Raman scattering (Renishaw 100, 632.8 nm He–Ne laser) were employed to determine the phase structure. The missing lattice atoms were observed by high-resolution HAADF-STEM and analyzed via intensity profile. The electronic states of Co and Fe before catalysis were studied by XPS (PHOIBOS 100 Analyzer from SPECS, Berlin, Germany; Al K_α X-rays), and those after CA test at $\eta = 370$ mV for 1.5 h were investigated by EELS (Gatan GIF Quantum ER EELS spectrometer). The EELS characterization was performed at liquid nitrogen temperature to avoid sample damaging and electronic-state changes, and the spectrometer was calibrated against the zero-loss peak at the start of each session. The deconvolution and curve-fitting of the spectra were performed by employing nonlinear least squares fitting tools written in DigitalMicrograph software. The coordination environments of Co and Fe before and after catalysis (CA test at $\eta = 320$ mV for 0.5 h) were also studied by XANES (National Synchrotron Radiation Laboratory (NSRL), Hefei, China). The Co and Fe L-edges XANES spectra of catalysts were measured at the photoemission end-station at beamline BL10B in the NSRL, Hefei, China. A bending magnet is connected to the beamline, which is equipped with three gratings covering photon energies from 100 to 1000 eV. The samples were kept in the total-electron-yield mode under an ultrahigh vacuum at 5×10^{-10} mbar. The resolving power of the grating was typically $E/\Delta E = 1000$, and the photon flux was 1×10^{10} photons per s. Spectra were collected at energies from 770 to 814 eV for Co and 695 to 740 eV for Fe in 0.2 eV energy steps. The XANES raw data were normalized by a procedure consisting of several steps.

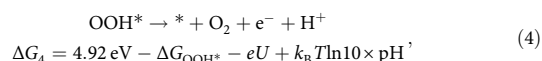
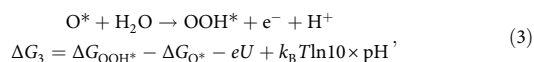
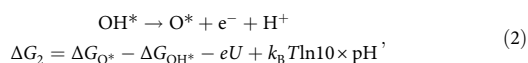
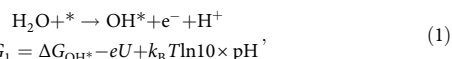
Electrochemical measurements. The catalytic performances were evaluated via the RDE method with continuous rotation at 1200 rpm (CHI 760, Shanghai Chenhua Instruments Co. Ltd.), where O₂-saturated 1 M NaOH, graphite rod and Hg/HgO electrode were utilized as the electrolyte, counter electrode and reference electrode, respectively. The working electrode was prepared by placing 12 μ l of catalyst suspension onto glassy carbon electrode which was dried in a fume

cupboard. The catalyst ink was prepared by suspending 2 mg catalyst in 1 ml water/isopropanol/Nafion® mixed solution (3:1:0.2, v/v) under ultrasonication. Before catalytic evaluation, the electrolyte was fully purified with the working electrode via CV cycles between 0.30 and 0.75 V vs. Hg/HgO at 10 mV s⁻¹ until a stable response was achieved. New working electrodes were then activated by six CV cycles, during which CoSe₂ was fully converted into CoOOH. LSV was then recorded within the voltage range of 0.30–1.00 V vs. Hg/HgO at 10 mV s⁻¹, and the polarization curves were corrected with 95% *i*R-compensation and then normalized by electrochemical double-layer capacitance that was estimated from the slope of the difference between anodic and cathodic current densities at 0.35 V vs. Hg/HgO against the scan rate (10, 20, 30, 40, 50, and 60 mV s⁻¹). After that, the electrodes were stabilized at 0.70 V vs. Hg/HgO for 3 min, and then electrochemical impedance spectroscopy was performed at the same potential with an amplitude of 10 mV and a frequency range of 200 kHz–100 mHz. The catalytic durability was finally assessed by CA test at stepwise potentials of 0.70, 0.75, 0.80, and 0.85 V vs. Hg/HgO for 6 h, and CP test at a constant current density of 10 mA cm⁻² for 8 h.

Overpotentials were determined by $\eta^{\text{OER}} = E_{\text{Hg/HgO}} + (0.098 + 0.059 \text{ pH} - 1.23) \text{ V}$, where $E_{\text{Hg/HgO}}$ is the recorded potential vs. Hg/HgO. TOF values were calculated based on $\text{TOF} = j/S/4Fn$, where j (A cm⁻²) is the current density at $\eta = 280$ mV, S (cm²) is the surface area of glassy carbon electrode, F is the Faraday constant (96,485 C mol⁻¹), and n is the number of moles of the cations assuming all of them are catalytically active. Tafel plots were derived from the polarization curves in low overpotential regions by plotting overpotential against log(current density). The error bars of reported overpotentials, current densities and TOFs were obtained from five replicates after discarding the maximum and minimum values.

Computational methods. In this work, the crystal structure of CoOOH was chosen to build up the periodical surfaces including Fe doping and Co/O vacancy models. The high-index (01-12) facet was adopted as the surface termination^{36,37}, as it exhibits theoretical activities in good agreement with the experimental results. The periodic surface was 14.79 Å × 15.22 Å with a vacuum slab of 18 Å in thickness to separate the layer from its periodic images. All the calculations were performed by spin-polarized plane-wave DFT, as implemented in the CASTEP program⁴³. The geometry optimizations were performed using the BFGS algorithm. The Perdew–Burke–Ernzerhof exchange-correlation functional within the generalized gradient approximation as well as ultrasoft pseudopotentials was selected^{44,45}. The cut-off energy for the plane-wave basis and the Brillouin zone *k*-points were chosen as 340.0 eV and 0.04 Å⁻¹ spacing in the Monkhorst–Pack scheme⁴⁶, respectively, which causes little difference in the calculation results when further increase. To sufficiently consider the on-site Coulombic repulsion between the *d* electrons, the Hubbard *U* corrections were applied to transition metal *d*-electrons and the values of *U*–*J* parameters for Co (3.42) and Fe (3.29) atoms were taken from the reference⁴⁷. The convergence criteria for the total energy, forces, stress, atomic displacement, and self-consistent field iterations were set to 1×10^{-5} eV atom⁻¹, 3×10^{-2} eV Å⁻¹, 5×10^{-2} GPa, 1×10^{-3} Å, and 1×10^{-6} eV atom⁻¹, respectively.

The OER reaction steps and Gibbs free energy changes can be expressed by³⁷



where * represents an active site on (01-12) facet, and ΔG_i ($i = \text{OH}^*$, O^* , and OOH^*) are Gibbs free energies of OER intermediates. The theoretical overpotential under standard conditions ($T = 298.15 \text{ K}$, $p = 1 \text{ bar}$, $\text{pH} = 0$) is then given by³⁷

$$\eta^{\text{OER}} = \max[\Delta G_1, \Delta G_2, \Delta G_3, \Delta G_4]/e - 1.23 \text{ V}. \quad (5)$$

The Gibbs free energies, ΔG_i , were determined by the adsorption energies combined with corrections for zero-point energy and entropy, according to $\Delta G_i = \Delta E_i + \Delta \text{ZPE}_i - T\Delta S_i$. The ZPE and TS were calculated using DFT calculations of vibrational frequencies and using standard tables for gas-phase molecules⁴⁸. The ZPEs for H₂, H₂O, *OH, *O, and *OOH are 0.27, 0.56, 0.35, 0.05, and 0.41 eV, respectively, and the TS corrections for H₂ and H₂O are 0.41 and 0.67 eV, respectively (we assume $S = 0$ for the adsorbates on coordinatively unsaturated sites). The adsorption energies of OER intermediates, ΔE_i ($i = \text{OH}^*$, O^* , and OOH^*), were calculated relative to H₂O and H₂ (at $U = 0$ and $\text{pH} = 0$)

$$\Delta E_{\text{OH}^*} = E_{\text{OH}^*} - E_* - (E_{\text{H}_2\text{O}} - 1/2E_{\text{H}_2}), \quad (6)$$

$$\Delta E_{\text{O}^*} = E_{\text{O}^*} - E_* - (E_{\text{H}_2\text{O}} - E_{\text{H}_2}), \quad (7)$$

$$\Delta E_{\text{OOH}^*} = E_{\text{OOH}^*} - E_* - (2E_{\text{H}_2\text{O}} - 3/2E_{\text{H}_2}). \quad (8)$$

The binding energies, ΔE_j ($j = \text{OH}, \text{O}, \text{and OOH}$), were calculated directly by $\Delta E_j = E_{j^*} - E_j - E_*$,

where * represents an active site on (01-12) facet, and E is the total energy calculated by using the spin polarization DFT method.

Data availability

The data that support the findings of this study are available from the corresponding author upon reasonable request.

Received: 8 October 2019; Accepted: 6 March 2020;

Published online: 03 April 2020

References

- Suen, N. T. et al. Electrocatalysis for the oxygen evolution reaction: recent development and future perspectives. *Chem. Soc. Rev.* **46**, 337–365 (2017).
- Wu, T. et al. Iron-facilitated dynamic active-site generation on spinel CoAl_2O_4 with self-termination of surface reconstruction for water oxidation. *Nat. Catal.* **2**, 763–772 (2019).
- Jin, H. et al. Emerging two-dimensional nanomaterials for electrocatalysis. *Chem. Rev.* **118**, 6337–6408 (2018).
- Pan, X., Yang, M. Q., Fu, X., Zhang, N. & Xu, Y. J. Defective TiO_2 with oxygen vacancies: synthesis, properties and photocatalytic applications. *Nanoscale* **5**, 3601–3614 (2013).
- Yan, J. et al. Single atom tungsten doped ultrathin $\alpha\text{-Ni}(\text{OH})_2$ for enhanced electrocatalytic water oxidation. *Nat. Commun.* **10**, 2149 (2019).
- Peng, S. et al. Necklace-like multishelled hollow spinel oxides with oxygen vacancies for efficient water electrolysis. *J. Am. Chem. Soc.* **140**, 13644–13653 (2018).
- Li, H. et al. Fe-doped CoSe_2 nanoparticles encapsulated in N-doped bamboo-like carbon nanotubes as an efficient electrocatalyst for oxygen evolution reaction. *Electrochim. Acta* **174**, 297–301 (2015).
- Zhang, J.-Y. et al. Rational design of cobalt-iron selenides for highly efficient electrochemical water oxidation. *ACS Appl. Mater. Interfaces* **9**, 33833–33840 (2017).
- Gao, M. R., Yao, W. T., Yao, H. B. & Yu, S. H. Synthesis of unique ultrathin lamellar mesostructured CoSe_2 -amine (protonated) nanobelts in a binary solution. *J. Am. Chem. Soc.* **131**, 7486–7487 (2009).
- Stevens, M. B. et al. Reactive Fe-sites in Ni/Fe (oxy)hydroxide are responsible for exceptional oxygen electrocatalysis activity. *J. Am. Chem. Soc.* **139**, 11361–11364 (2017).
- Chang, A., Zhang, C., Yu, Y., Yu, Y. & Zhang, B. Plasma-assisted synthesis of NiSe_2 ultrathin porous nanosheets with selenium vacancies for supercapacitor. *ACS Appl. Mater. Interfaces* **10**, 41861–41865 (2018).
- Liu, Y. et al. Low overpotential in vacancy-rich ultrathin CoSe_2 nanosheets for water oxidation. *J. Am. Chem. Soc.* **136**, 15670–15675 (2014).
- Zheng, Y. R. et al. Doping-induced structural phase transition in cobalt diselenide enables enhanced hydrogen evolution catalysis. *Nat. Commun.* **9**, 2533 (2018).
- Gui, Y. et al. Manipulating the assembled structure of atomically thin CoSe_2 nanomaterials for enhanced water oxidation catalysis. *Nano Energy* **57**, 371–378 (2019).
- Dou, Y. et al. Atomic layer-by-layer Co_3O_4 /graphene composite for high performance lithium-ion batteries. *Adv. Energy Mater.* **6**, 1501835 (2016).
- Lesnyak, V., Brescia, R., Messina, G. C. & Manna, L. Cu vacancies boost cation exchange reactions in copper selenide nanocrystals. *J. Am. Chem. Soc.* **137**, 9315–9323 (2015).
- Zhou, Q. et al. Active-site-enriched iron-doped nickel/cobalt hydroxide nanosheets for enhanced oxygen evolution reaction. *ACS Catal.* **8**, 5382–5390 (2018).
- Zheng, Y. R. et al. An efficient $\text{CeO}_2/\text{CoSe}_2$ nanobelt composite for electrochemical water oxidation. *Small* **11**, 182–188 (2015).
- Zhou, Y. et al. Co_3O_4 @(Fe-doped) $\text{Co}(\text{OH})_2$ microfibers: facile synthesis, oriented-assembly, formation mechanism, and high electrocatalytic activity. *ACS Appl. Mater. Interfaces* **9**, 30880–30890 (2017).
- Zhao, X. et al. Engineering the electrical conductivity of lamellar silver-doped cobalt(II) selenide nanobelts for enhanced oxygen evolution. *Angew. Chem. Int. Ed.* **56**, 328–332 (2017).
- Jin, H. et al. Fe incorporated $\alpha\text{-Co}(\text{OH})_2$ nanosheets with remarkably improved activity towards the oxygen evolution reaction. *J. Mater. Chem. A* **5**, 1078–1084 (2017).
- Li, J. et al. Fe-doped CoSe_2 nanoparticles encapsulated in N-doped bamboo-like carbon nanotubes as an efficient electrocatalyst for oxygen evolution reaction. *Electrochim. Acta* **265**, 577–585 (2018).
- Liang, L. et al. Metallic single-unit-cell orthorhombic cobalt diselenide atomic layers: robust water-electrolysis catalysts. *Angew. Chem. Int. Ed.* **54**, 12004–12008 (2015).
- Gao, M. R. et al. CoSe_2 nanobelts composite catalyst for efficient water oxidation. *ACS Nano* **8**, 3970–3978 (2014).
- Xu, H. et al. Phosphorus-doped cobalt-iron oxyhydroxide with untrafine nanosheet structure enable efficient oxygen evolution electrocatalysis. *J. Colloid Interface Sci.* **530**, 58–66 (2018).
- Zhang, L. et al. Ultrathin iron-cobalt oxide nanosheets with abundant oxygen vacancies for the oxygen evolution reaction. *Adv. Mater.* **29**, 1606793 (2017).
- Xiao, C., Lu, X. & Zhao, C. Unusual synergistic effects upon incorporation of Fe and/or Ni into mesoporous Co_3O_4 for enhanced oxygen evolution. *Chem. Commun.* **50**, 10122–10125 (2014).
- Gao, M. R., Xu, Y. F., Jiang, J., Zheng, Y. R. & Yu, S. H. Water oxidation electrocatalyzed by an efficient $\text{Mn}_3\text{O}_4/\text{CoSe}_2$ nanocomposite. *J. Am. Chem. Soc.* **134**, 2930–2933 (2012).
- Li, N. et al. Influence of iron doping on tetravalent nickel content in catalytic oxygen evolving films. *Proc. Natl Acad. Sci. USA* **114**, 1486–1491 (2017).
- Jiang, H., He, Q., Zhang, Y. & Song, L. Structural self-reconstruction of catalysts in electrocatalysis. *Acc. Chem. Res.* **51**, 2968–2977 (2018).
- Guo, C. et al. Engineering high-energy interfacial structures for high-performance oxygen-involving electrocatalysis. *Angew. Chem. Int. Ed.* **56**, 8539–8543 (2017).
- Zhang, S. et al. Determination of manganese valence states in (Mn^{3+} , Mn^{4+}) minerals by electron energy-loss spectroscopy. *Am. Mineral.* **95**, 1741–1746 (2010).
- Ling, T. et al. Activating cobalt(II) oxide nanorods for efficient electrocatalysis by strain engineering. *Nat. Commun.* **8**, 1509 (2017).
- Cheng, J. et al. Enhanced insulating behavior in the Ir-vacant $\text{Sr}_2\text{Ir}_{1-x}\text{O}_4$ system dominated by the local structure distortion. *J. Synchrotron Rad.* **25**, 1123 (2018).
- Cao, L. et al. Identification of single-atom active sites in carbon-based cobalt catalysts during electrocatalytic hydrogen evolution. *Nat. Catal.* **2**, 134 (2019).
- Bajdich, M., García-Mota, M., Vojvodic, A., Nørskov, J. K. & Bell, A. T. Theoretical investigation of the activity of cobalt oxides for the electrochemical oxidation of water. *J. Am. Chem. Soc.* **135**, 13521–13530 (2013).
- Friebel, D. et al. Identification of highly active Fe sites in (Ni,Fe)OOH for electrocatalytic water splitting. *J. Am. Chem. Soc.* **137**, 1305–1313 (2015).
- Man, I. C. et al. Universality in oxygen evolution electrocatalysis on oxide surfaces. *ChemCatChem* **3**, 1159–1165 (2011).
- Burke, M. S. et al. Cobalt-iron (oxy)hydroxide oxygen evolution electrocatalysts: the role of structure and composition on activity, stability, and mechanism. *J. Am. Chem. Soc.* **137**, 3638–3648 (2015).
- Smith, R. D. L. et al. Spectroscopic identification of active sites for the oxygen evolution reaction on iron-cobalt oxides. *Nat. Commun.* **8**, 2022 (2017).
- Zhang, B. et al. Homogeneously dispersed multimetal oxygen-evolving catalysts. *Science* **352**, 333–337 (2016).
- Qiu, B. et al. Fabrication of nickel-cobalt bimetal phosphide nanocages for enhanced oxygen evolution catalysis. *Adv. Funct. Mater.* **28**, 1706008 (2018).
- Clark, S. J. et al. First principles methods using CASTEP. *Z. Kristallogr.* **220**, 567–570 (2005).
- Vanderbilt, D. et al. Soft self-consistent pseudopotentials in a generalized eigenvalue formalism. *Phys. Rev. B* **41**, 7892–7895 (1990).
- Perdew, J. P., Burke, K. & Ernzerhof, M. Generalized gradient approximation made simple. *Phys. Rev. Lett.* **77**, 3865–3868 (1996).
- Monkhorst, H. J. & Park, J. D. Special points for Brillouin-zone intergrations. *Phys. Rev. B* **13**, 5188–5192 (1976).
- Xu, H., Cheng, D., Cao, D. & Zeng, X. C. A universal principle for a rational design of single-atom electrocatalysts. *Nat. Catal.* **1**, 339–348 (2018).
- Valdés, Á., Qu, Z. W., Kroes, G. J., Rossmeisl, J. & Nørskov, J. K. Oxidation and photo-oxidation of water on TiO_2 surface. *J. Phys. Chem. C* **112**, 9872–9879 (2008).

Acknowledgements

This work is financially supported by an Australian Research Council (ARC) Discovery Projects (DP200100965) and a Griffith University Postdoctoral Fellowship (YUDOU 036 Research Internal). The authors are grateful to Dr David Mitchell and Dr Ningyan Cheng from UOW Electron Microscopy Centre for their assistance in STEM work.

Author contributions

Y.D. conceived the idea, carried out the experiment, and wrote the paper. H.Z. provided research facilities, financial support, and valuable suggestions for the experiment and paper writing. C.T.H. performed the DFT calculations. L.Z. and H.Y. participated in the data analysis and discussion. M.A. and J.M. provided assistance in XRD, XPS, and STEM characterizations.

Competing interests

The authors declare no competing interests.

Additional information

Supplementary information is available for this paper at <https://doi.org/10.1038/s41467-020-15498-0>.

Correspondence and requests for materials should be addressed to H.Z.

Peer review information *Nature Communications* thanks the anonymous reviewers for their contributions to the peer review of this work.

Reprints and permission information is available at <http://www.nature.com/reprints>

Publisher's note Springer Nature remains neutral with regard to jurisdictional claims in published maps and institutional affiliations.



Open Access This article is licensed under a Creative Commons Attribution 4.0 International License, which permits use, sharing, adaptation, distribution and reproduction in any medium or format, as long as you give appropriate credit to the original author(s) and the source, provide a link to the Creative Commons license, and indicate if changes were made. The images or other third party material in this article are included in the article's Creative Commons license, unless indicated otherwise in a credit line to the material. If material is not included in the article's Creative Commons license and your intended use is not permitted by statutory regulation or exceeds the permitted use, you will need to obtain permission directly from the copyright holder. To view a copy of this license, visit <http://creativecommons.org/licenses/by/4.0/>.

© The Author(s) 2020